

# On the Origin of Anode and Cathode Contributions to the Impedance of All-Solid-State Batteries

Christoph König,<sup>[a]</sup> Asvitha Ramanayagam,<sup>[a]</sup> Jennifer Kraus,<sup>[a]</sup> and Bernhard Roling<sup>\*[a]</sup>

All-solid-state-batteries (ASSBs) are considered as promising next-generation batteries in order to achieve improvements in both energy density and safety. The complex electrochemical processes in ASSBs taking place on different time scales can be probed by means of electrochemical impedance spectroscopy. However, the separation of anode and cathode contributions to the impedance and the understanding of the underlying electrochemical processes in both electrodes is a challenging task. Here, we compare the impedance spectrum of a prototypical full ASSB to those of symmetric cells anode | separator |

anode and cathode | separator | cathode. We use Ni-rich polycrystalline  $\text{LiNi}_{0.85}\text{Co}_{0.10}\text{Mn}_{0.05}\text{O}_2$  particles as active material inside the composite cathode and an indium-lithium alloy as anode. Based on the comparison, we show that the charge transfer process inside the cathode is remarkably fast, i.e., even faster than observed for cathodes of batteries with liquid electrolyte. Our results give indication that the differences in the time scales of cathode and anode processes are related to the distinct transport properties of interphases inside the cathode and at the anode | separator interface, respectively.

## Introduction

In order to stop global warming,  $\text{CO}_2$  emissions have to be reduced drastically.<sup>[1,2]</sup> To this end, the production of renewable energy has to be increased, stationary energy storage devices have to be installed, and the electrification of the transport sector has to be pursued. Lithium-ion batteries (LIBs) play an important role for stationary as well as for mobile energy storage.<sup>[3–5]</sup> LIBs exhibit high energy and power densities,<sup>[6,7]</sup> however, they are slowly reaching the physicochemical limit of energy density. In addition, the usage of flammable liquid electrolytes in LIBs is a safety hazard.<sup>[8,9]</sup> All-solid-state batteries are currently considered as promising next-generation batteries in order to achieve improvements in both energy density and safety. The replacement of liquid electrolytes by solid electrolytes (SEs)<sup>[10,11]</sup> allows potentially for using metallic lithium as anode material<sup>[12–14]</sup> and also reduces the risk of battery fires.<sup>[15–17]</sup> Solid electrolytes can be categorized into different classes, such as oxides, halides, polymers and sulfides, whereby multinary sulfide-based SEs exhibit the highest room-temperature ionic conductivities.<sup>[18–20]</sup> In combination with a lithium-metal-based anode and a Ni-rich cathode active material (CAM), energy densities exceeding those of LIBs considerably are potentially achievable.<sup>[21,22]</sup> Nevertheless, ASSBs still need improvements in cycle stability.<sup>[23,24]</sup>

The understanding of the complex electrochemical processes in ASSBs is a key factor for further improving ASSBs. Electrochemical impedance spectroscopy (EIS) is an important technique for analyzing the impedance contributions of different processes taking place on different time scales. In the case of LIBs, the usage of reference electrodes in battery cells is a straightforward method for separating, in a first step, the anode impedance from the cathode impedance. In the case of ASSBs, the usage of a reference electrode is challenging, since high impedances between the reference electrode and the solid electrolyte can produce reference electrode artifacts at high frequencies in the impedance spectra.<sup>[25,26]</sup> Nevertheless, 3-electrode measurements were carried out successfully and yielded satisfactory results at low and intermediate frequencies.<sup>[27,28]</sup> However, most impedance spectra of ASSBs were taken in a two-electrode configuration, thus containing contributions from both anode and cathode. The differentiation between these contributions has been discussed in several publications. There is indication that the impedance semicircle originating from ion transport and charge transfer processes inside the composite cathode occurs at higher frequencies as compared to the charge transfer semicircle of the anode.<sup>[29–32]</sup> However, the opposite finding has also been reported.<sup>[33]</sup> In a previous work, we compared the impedance spectra of ASSBs with those of symmetrical cells anode | separator | anode and found indication for a cathode semicircle showing up in a frequency range from  $10^5$  to  $10^3$  Hz and an anode semicircle showing up at lower frequencies in a range from  $10^2$  to  $10^{-1}$  Hz.<sup>[34]</sup>

Here, we present the results of complementary experiments, in which we built two types of symmetrical cells, namely composite cathode | separator | composite cathode and anode | separator | anode. The symmetrical cells composite cathode | separator | composite cathode were constructed from two ASSBs both being in a state of charge of 50% (SOC50). We chose SOC50 in order to achieve cathodes with low charge transfer resistances. In this context, it is important to note that

[a] C. König, A. Ramanayagam, J. Kraus, B. Roling

Department of Chemistry, Philipps-Universität Marburg, Hans-Meerwein-Straße 4, D-35032 Marburg, Germany  
E-mail: roling@staff.uni-marburg.de

 Supporting information for this article is available on the WWW under <https://doi.org/10.1002/batt.202300578>

 © 2024 The Authors. *Batteries & Supercaps* published by Wiley-VCH GmbH. This is an open access article under the terms of the Creative Commons Attribution Non-Commercial License, which permits use, distribution and reproduction in any medium, provided the original work is properly cited and is not used for commercial purposes.

literature studies on composite cathode in a 3-electrode setup revealed qualitatively similar impedance spectra at different SOC values, suggesting that the origin of the impedance semicircles does not depend on the SOC.<sup>[28,29,31]</sup> Only at SOCs close to 0% and 100%, the spectral shape changes significantly. Impedance measurements at SOC0 have already been reported in the literature in order to obtain information about ionic and electronic tortuosities in composite cathodes.<sup>[35,36]</sup>

We compare the impedance of these symmetrical cells to those of full ASSBs also being in SOC50. The studies are carried out under two different pressures applied to the symmetrical cells and to the full ASSBs. As solid electrolyte in the cathode and as separator, we use the highly conductive glass-ceramic (gc) sulfide-based solid electrolyte  $\text{Li}_{5.3}\text{PS}_{4.3}\text{ClBr}_{0.7}$  (LPSCIBr<sub>0.7</sub>). The term "glass-ceramic" implies the existence of nanocrystallites in an amorphous matrix. The cathode and the anode active material are polycrystalline  $\text{LiNi}_{0.85}\text{Co}_{0.10}\text{Mn}_{0.05}\text{O}_2$  particles and an indium-lithium alloy, respectively. The indium-lithium alloy was chosen, since pressure up to 500 MPa can be applied, while Li metal anodes can only be used up to about 100 MPa.<sup>[37,38]</sup> After separating the impedance contributions of anode and cathode, we discuss the origin of these contributions showing up in different frequency ranges.

## Experimental Section

All experimental procedures were carried out in an argon-filled glovebox (Unilab, MBraun, Garching, Germany) with  $x_{\text{H}_2\text{O}} < 1 \text{ ppm}$  and  $x_{\text{O}_2} < 1 \text{ ppm}$ .

$\text{Li}_{5.3}\text{PS}_{4.3}\text{ClBr}_{0.7}$  (LPSCIBr<sub>0.7</sub>) glass-ceramic (gc) solid electrolyte was synthesized in a planetary ball mill (Pulverisette 7 premium line, Fritsch, Idar-Oberstein, Germany) by high-energy dry ball milling (HDM). For the synthesis of a 2 g batch of the electrolyte, a stoichiometric mixture of  $\text{Li}_2\text{S}$  (99.9%, Alfa Aesar, Karlsruhe, Germany),  $\text{P}_2\text{S}_5$  (for synthesis, Sigma-Aldrich, Taufkirchen, Germany),  $\text{LiCl}$  ( $\geq 99.98\%$ , Sigma-Aldrich, Taufkirchen, Germany) and  $\text{LiBr}$  ( $\geq 99.9\%$ , Sigma-Aldrich, Taufkirchen, Germany) powder were mixed in a 20 mL zirconia pot with 10 zirconia balls ( $\varnothing = 10 \text{ mm}$ ). The milling time was 8.25 h (99 cycles; 5 min milling; 15 min rest) with a rotation speed of 850 rpm. After milling, the electrolyte was grinded in an agate mortar to obtain a yellow to beige powder.

XRD measurement was performed using a powder diffractometer STOE STADI MP (STOE, Darmstadt, Germany) using  $\text{Cu K}\alpha$  radiation in a Debye–Scherrer geometry. The electrolyte powder was filled into a mark tube (Hilgenberg, Malsfeld, Germany) under argon, and the tube was closed airtight with wax.

For the ion conductivity measurement, 100 mg of the as-prepared solid electrolyte powder was filled into an all-solid-state battery cell (CompreCell, rhd instruments, Darmstadt, Germany), and the cell was integrated into a CompreDrive automated die press (rhd instruments, Darmstadt, Germany). A solid electrolyte pellet was prepared by applying a fabrication pressure of 392 MPa for 90 s. During the measurement, a stack pressure of 98 MPa was applied, and the impedance was measured by a potentiostat/galvanostat Autolab PGSTAT302 N (Methrom Autolab, Utrecht, the Netherlands). The frequency range extended from  $10^5$  to  $10^1 \text{ Hz}$  with an applied AC voltage of  $10 \text{ mV}_{\text{rms}}$ . The temperature range was chosen from 85 to 30 °C in 5 °C steps. The obtained temperature-dependent conductivity data were fitted in an Arrhenius plot, and the fit was extrapolated to 25 °C.

The composite cathode was prepared in an agate mortar by mixing the CAM particles and the SE particles with a mass ratio of 70:30 for 15 min. Polycrystalline  $\text{LiNi}_{0.85}\text{Co}_{0.10}\text{Mn}_{0.05}\text{O}_2$  particles (NCM851005, BASF SE, Ludwigshafen, Germany) with a typical particle size of  $D_{50} = 2.42 \mu\text{m}$  (particle size distribution is shown in Figure S4) were used as CAM. These particles were coated with  $\text{LiNbO}_3$  (1 wt %) by means of a sol-gel process described in Ref. [39,40].

The preparation of the ASSB and the electrochemical measurements were carried out using the CompreDrive automated die press (rhd instruments, Darmstadt, Germany) in an active force control mode. First, 50 mg gc LPSCIBr<sub>0.7</sub> (HDM) electrolyte powder was filled into an all-solid-state battery cell (CompreCell, rhd instruments, Darmstadt, Germany) and was pressed with an applied pressure of 98 MPa for 90 s using wolfram carbide pistons to prepare a separator layer. Both pistons were removed, and on one side of the separator layer, 30 mg of the composite cathode mixture, and on the other side, 35 mg indium foil (99.99%, Carl Roth, Karlsruhe, Germany) with a diameter of 12 mm were added. The entire ASSB was then compressed using a fabrication pressure of 392 MPa. The electrochemical measurements on the ASSB were carried out using the potentiostat/galvanostat Autolab PGSTAT302 N (Methrom Autolab, Utrecht, The Netherlands). The galvanostatic cycling studies were done at a stack pressure of 392 MPa at room temperature and at a rate of 0.1 C. The cutoff voltages were chosen as 3.9 V and 2.5 V, respectively. First, a complete charge/discharge cycle was finalized, before the ASSB was charged to a state of charge of 50% (SOC50) using 50% of the discharge capacity in the first cycle. The impedance measurement was carried out after a relaxation time of 24 h at the open circuit potential in a frequency range from  $10^5$  to  $10^{-3} \text{ Hz}$  with an applied AC voltage of  $10 \text{ mV}_{\text{rms}}$  and a stack pressure of 392 MPa.

The preparation procedure for both types of symmetric cells is illustrated in Figure S11. For the symmetric cell composite cathode | separator | composite cathode, as sketched in Figure 1a, two full ASSBs were prepared in two PEEK tubes with two slightly different diameters ( $\varnothing = 10 \text{ mm}$  and  $10.6 \text{ mm}$ , respectively) and charged to SOC50 as follows: First, 150 mg gc LPSCIBr<sub>0.7</sub> (HDM) electrolyte powder was compressed at a fabrication pressure of 98 MPa in order to prepare a separator layer. Then 20 mg of the cathode mixture was added on one side of the separator layer. On the other side, 25 mg indium foil (99.99%, Carl Roth, Karlsruhe, Germany) with a diameter of 10 mm or  $10.6 \text{ mm}$  was added. The full ASSBs were then compressed using a fabrication pressure of 392 MPa. Thereafter, the ASSBs were cycled to a state of charge of 50% at a stack pressure of 98 MPa. After cycling, the anode of both ASSBs was removed by mechanical scratching and the composite cathode | separator pellet inside the PEEK tube with the slightly lower diameter was pressed out of the PEEK tube. The composite cathode | separator pellet in the other PEEK tube with the slightly larger diameter was overlaid with a tiny amount (15 mg) of SE powder in order to compensate for the rough LPSCIBr<sub>0.7</sub> separator surface after removal of the anode. Then, the second pellet was placed on top of the SE powder layer to form a composite cathode | separator | composite cathode cell. During the entire preparation of the symmetric cell, self-discharge of the cathode cannot take place, since the cathode is always covered by a solid electrolyte separator layer inhibiting electronic contact to other layers.

The cell was pressed in the atlas manual hydraulic press 25T (Specac, Orpington, England) with a pressure of 98 MPa, and after the first impedance measurement, the cell was compressed with a pressure of 392 MPa, at which the second impedance measurement was carried out. All electrochemical measurements on the full ASSBs and on the symmetrical cell were carried out using the potentiostat/galvanostat BioLogic SP-150 (BioLogic, Grenoble,

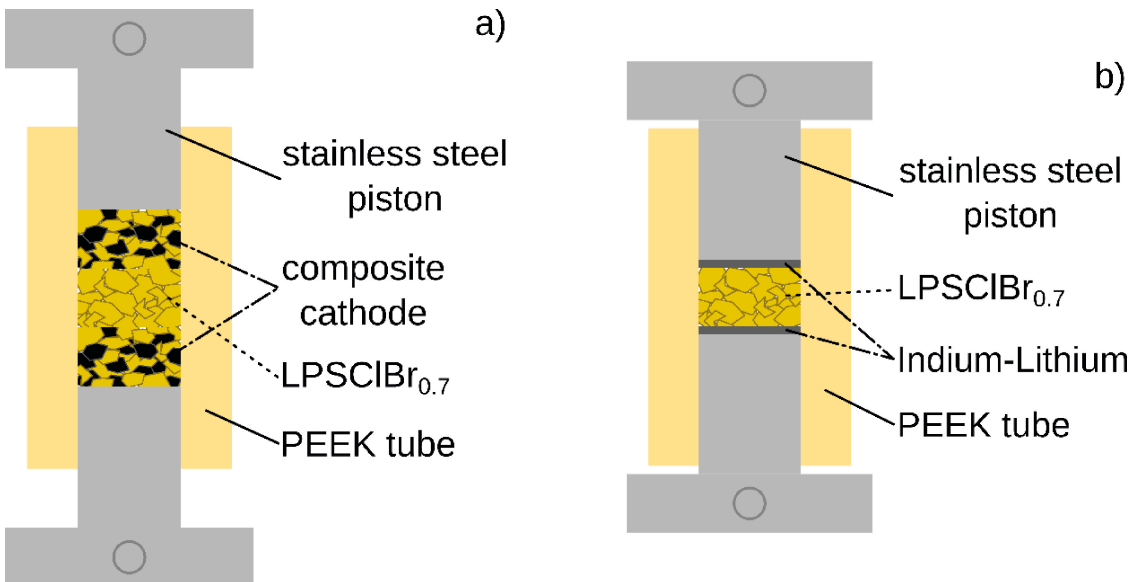


**Figure 1.** Schematic illustration of symmetrical cells a) composite cathode | separator | composite cathode, b) In–Li | separator | In–Li between two stainless steel pistons (home-built cell).

France). The galvanostatic cycling studies were carried out at a stack pressure of 98 MPa at room temperature and at a rate of 0.1 C. The cutoff voltages and the impedance measurement parameters were identical to the measurements in the Compre-Drive automated die press.

For the symmetric cell In–Li | separator | In–Li, as sketched in Figure 1b, two ASSBs were prepared by using the same procedure as for the symmetric cell composite cathode | separator | composite cathode, except that the cathode was removed instead of the anode, see Figure S11. The used PEEK tubes had two slightly different diameters of  $\varnothing=10$  mm and 10.2 mm, respectively, and the two ASSBs were charged to a state, at which the In:Li ratio in the anode was 60:40. The symmetrical cell was compressed in the atlas manual hydraulic press 25T (Specac, Orpington, England) with a pressure of 98 MPa.

The galvanostatic cycling studies on the ASSBs were carried out using the potentiostat/galvanostat BioLogic SP-150 (BioLogic, Grenoble, France) at a stack pressure of 98 MPa at room temperature and at a rate of 0.1 C. The cutoff voltages were chosen as 3.9 V and 2.5 V, respectively. The impedance measurement on the symmetrical cell was carried out at a stack pressure of 98 MPa using the NEISYS electrochemical impedance analyzer (Novocontrol, Montabaur, Germany) in a frequency range from  $10^6$  to  $10^{-2}$  Hz with an applied AC voltage of 10 mV<sub>rms</sub>. The impedance spectra were analyzed by means of the software RelaxIS (rhd instruments, Darmstadt, Germany).

SEM images of the cathode active material particles were taken with a focused ion beam/secondary electron microscope (FIB-SEM; crossbeam 550, Zeiss, Oberkochen, Germany). For transferring the samples under inert gas conditions from the glovebox to the FIB-SEM, a sample transfer shuttle (Semilab Semiconductor Physics Laboratory Co. Ltd., Budapest, Hungary) was used.

## Results and Discussion

In Figure 2a and b, we show the impedance spectra of a symmetrical cell composite cathode | separator | composite cathode taken at a stack pressure of 98 MPa and 392 MPa, respectively, with the CAM being in a state of charge of 50% (SOC50). At high frequencies, the spectra are dominated by the resistance of the solid-electrolyte separator and the inductance of the connecting cables. At intermediate frequencies ranging from  $10^5$  Hz to  $10^1$  Hz, the spectra show a semicircle, which can be attributed to ion transport in the SE particles in the composite electrode and the charge transfer at the interface between the CAM particle and the SE particles. At low frequencies, a Warburg-open-type impedance is observed, which is caused by chemical Li diffusion in the CAM particles and by the chemical capacitance of the CAM particles. The spectral shape is in good agreement with the data of Hori et al.<sup>[31]</sup> who used LiCoO<sub>2</sub> at SOC100 as CAM together with a sulfide-based solid electrolyte.

In order to obtain the impedance of a single cathode from the spectra in Figure 2a and b, the high-frequency part of the spectra was fitted by an equivalent circuit suitable for obtaining the separator resistance  $R_{\text{separator}}$  and the cable inductance  $L$ . The separator resistance  $R_{\text{separator}}$  and the inductive impedance  $i\omega L$  were subtracted from the spectra, and the resulting impedance was halved to obtain the impedance of a single electrode. The exact procedure is described in the supporting information and shown in Figure S6.

Figure 3a and b show the impedance spectra of a single cathode contribution at a stack pressure of 98 MPa and 392 MPa, respectively. When the pressure is increased by a factor of 4, the diameter of the semicircle reduces from  $10.8 \Omega \cdot \text{cm}^2$  to  $4.3 \Omega \cdot \text{cm}^2$  and also the Warburg-open-type impedance is reduced. For a more detailed analysis of the

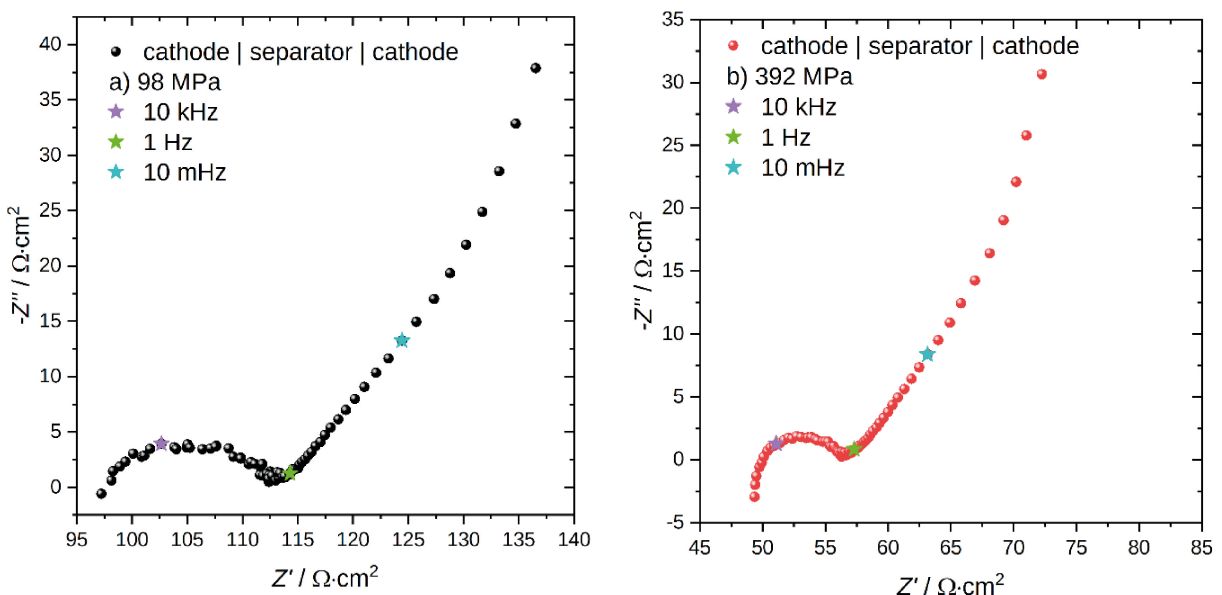


**Figure 2.** Impedance spectra of a symmetrical cell composite cathode | separator | composite cathode at a stack pressure of a) 98 MPa and b) 392 MPa, respectively. Both composite cathodes are in a state of charge of 50% (SOC50).

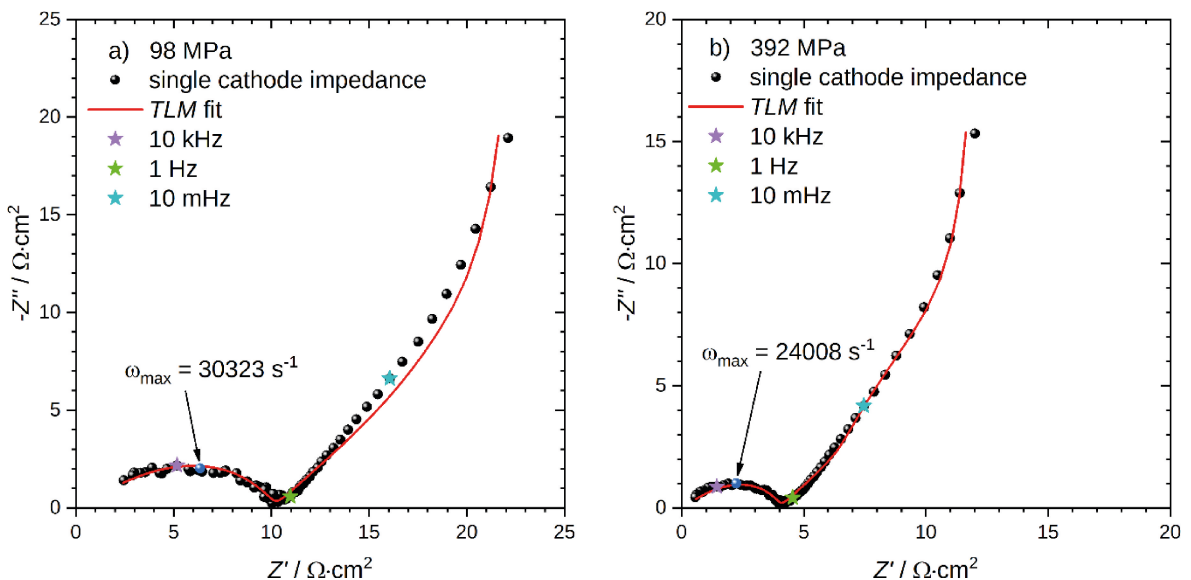


**Figure 3.** Single cathode impedance (SOC50) and fit with the transmission-line model at a stack pressure of a) 98 MPa and b) 392 MPa, respectively.

cathode impedance, the spectra were fitted by a transmission-line model (TLM) for composite electrodes with negligible electronic resistance. This TLM is applicable, if the electronic resistance of the composite electrode is much lower than the ionic resistance. For different NCM stoichiometries (NCM622, NCM811 and NCM831106), the electronic conductivity at a state of charge of 0% (SOC0) is above 1 mS/cm.<sup>[34,41]</sup> At SOC50, no values for the electronic conductivity are available in the literature, but it is reasonable to assume that the electronic conductivity of NCM at SOC50 is at least as high as that of LCO at SOC50, which is >100 mS/cm.<sup>[42]</sup> This assumption is supported by measurements of NCM composite cathodes at SOC0 in a setup metal | composite cathode | metal, showing

that the electronic conductivity is much higher than the ionic conductivity.<sup>[34,36]</sup> The prerequisite for the applicability of the TLM with negligible electronic resistance is thus fulfilled.

In the framework of this TLM, the impedance of the cathode is given by:<sup>[32]</sup>

$$Z_{\text{cathode}} = \sqrt{\frac{Z_{\text{loc}} \cdot R_{\text{ion}}}{a_v \cdot d}} \cdot \coth\left(\sqrt{\frac{R_{\text{ion}} \cdot a_v \cdot d}{Z_{\text{loc}}}}\right) \quad (1)$$

with

$$R_{\text{ion}} = \frac{\tau_{\text{Li}^+} \cdot d}{\varepsilon_{\text{SE}} \cdot \sigma} \quad (2)$$

$$Z_{\text{loc}} = \left( \frac{1}{R_{\text{CT}} + \frac{dU}{dc_{\text{Li}}} \cdot Y_{\text{CAM}}} + (i\omega)^{\beta} \cdot Q_{\text{DL}} \right)^{-1} \quad (3)$$

and with

$$Y_{\text{CAM}} = \frac{r_{\text{CAM}}}{F \cdot D_{\text{CAM}}} \cdot \frac{\tanh\left(\sqrt{\frac{i\omega \cdot r_{\text{CAM}}^2}{D_{\text{CAM}}}}\right)}{\tanh\left(\sqrt{\frac{i\omega \cdot r_{\text{CAM}}^2}{D_{\text{CAM}}}}\right) - \sqrt{\frac{i\omega \cdot r_{\text{CAM}}^2}{D_{\text{CAM}}}}} \quad (4)$$

Here,  $R_{\text{ion}}$  denotes the ion transport resistance of the composite cathode,  $d$  its thickness,  $\sigma_{\text{ion}}$  the ionic conductivity of the SE,  $\varepsilon_{\text{SE}}$  the volume fraction of the SE in the cathode, and  $\tau_{\text{Li}^+}$  the tortuosity of the  $\text{Li}^+$  ion transport within the composite cathode.  $Z_{\text{loc}}$  is the local impedance due to double layer formation and charge transfer at the CAM | SE interface, due to Li chemical diffusion in the CAM particles and due to the chemical capacitance of the CAM particles.  $R_{\text{CT}}$  denotes the charge transport resistance,  $dU/dc_{\text{Li}}$  the dependence of equilibrium electrode potential on the lithium concentration in the CAM,  $Y_{\text{CAM}}$  the frequency dependence of Li chemical diffusion in the CAM particles, and  $(i\omega)^{\beta} Q_{\text{DL}}$  with  $\beta < 1$  the non-ideal double layer capacitance.<sup>[34]</sup>  $a_v$  is the active area of the CAM particles in contact to the SE normalized to the cathode volume

$$a_v = \frac{\varepsilon_{\text{CAM}} \cdot A_{\text{CAM}}}{V_{\text{CAM}}} = \frac{3\varepsilon_{\text{CAM}}}{r_{\text{CAM}}} \quad (5)$$

with  $\varepsilon_{\text{CAM}}$ ,  $A_{\text{CAM}}$ ,  $V_{\text{CAM}}$  and  $r_{\text{CAM}}$  denoting the volume fraction, surface area, volume and radius of the CAM particles, respectively.  $D_{\text{CAM}}$  is the lithium chemical diffusion coefficient in the CAM particles, and  $F$  the Faraday constant. The charge transfer resistance is related to the  $\text{Li}^+$  exchange current density at the CAM | SE interface,  $j_0$ , via:

$$R_{\text{CT}} = \frac{R \cdot T}{F \cdot j_0} \quad (6)$$

Here,  $R$  and  $T$  are the ideal gas constant and the temperature, respectively.

Most of the TLM parameters needed for fitting the experimental data are either known from the literature or can be determined from supporting measurements, see Table 1. The thickness  $d$  of the composite cathode as well as the volume fractions of cathode active material  $\varepsilon_{\text{CAM}}$  and solid electrolyte  $\varepsilon_{\text{SE}}$  were taken from the literature, since in Ref. [36], the same fabrication pressure and the same mass ratio of the particles was used. The average radius (D50 value) of the CAM particles,  $r_{\text{CAM}}$ , was calculated from the particle size distribution determined from SEM images, see Figures S3 and S4. The Li diffusion coefficient,  $D_{\text{CAM}}$ , was taken from the literature.<sup>[43,44]</sup> A starting value for the tortuosity of the ion transport,  $\tau_{\text{Li}^+}$ , was taken from

**Table 1.** Fixed parameters in the TLM fit of the single cathode impedance spectra (SOC50) at both stack pressures (98 MPa and 392 MPa).

parameter	symbol	value	unit
temperature	$T$	298	K
area of the cell	$A$	$8.82 \cdot 10^{-5}$	$\text{m}^2$
ionic conductivity of SE	$\sigma$	0.409	$\text{S} \cdot \text{m}^{-1}$
thickness of the composite cathode	$d$	$7.71 \cdot 10^{-5}$	m
volume fraction of SE particles	$\varepsilon_{\text{SE}}$	0.450	-
volume fraction of CAM particles	$\varepsilon_{\text{CAM}}$	0.439	-
average radius of the CAM particles	$r_{\text{CAM}}$	$2.42 \cdot 10^{-6}$	m
tortuosity of ion transport	$\tau_{\text{Li}^+}$	7.8	-

the literature,<sup>[36]</sup> and a starting value for  $dU/dc_{\text{Li}}$  was calculated from the slope of the charge/discharge curve at a very low cycling rate of C/30, see Figure S5. Three parameters were taken as freely adjustable, namely  $j_0$ ,  $Q_{\text{DL}}$  and  $\beta$ .

In Figure 3a and b, we show the TLM fit of the experimental data at a stack pressure of 98 MPa and of 392 MPa, respectively. Overall, there is good agreement between data and fit. At 98 MPa, there are slight deviations between data and fit in the Warburg-open regime. The fit parameters are given in Table 2. We note that exchange current density exhibits high values of  $j_0 = 2.0 \text{ A} \cdot \text{m}^{-2}$  and  $12.3 \text{ A} \cdot \text{m}^{-2}$  for a stack pressure of 98 MPa and 392 MPa, respectively. These values are in the same range as values obtained for NCM622 particles in contact with a liquid electrolyte ( $j_0 = 2-5 \text{ A} \cdot \text{m}^{-2}$ ).<sup>[45]</sup> The double layer capacitance at the CAM | SE interface was estimated from the angular frequency of the  $Z''$  maximum of the semicircle,  $\omega_{\text{max}}$ , and the charge transfer resistance  $R_{\text{CT}}$  using the equation:

**Table 2.** Variable parameters in the TLM fit of the single cathode impedance spectra (SOC50).

parameter	symbol	value	unit
stack pressure 98 MPa			
exchange current density	$j_0$	2.0	$\text{A} \cdot \text{m}^{-2}$
dependence of equilibrium potential on Li concentration in CAM	$dU/dc_{\text{Li}}$	$-5.4 \cdot 10^{-5}$	$\text{V} \cdot \text{m}^3 \cdot \text{mol}^{-1}$
prefactor of double layer CPE	$Q_{\text{DL}}$	0.15	$\text{F} \cdot \text{m}^{-2} \cdot \text{s}^{\beta-1}$
exponent of double layer CPE	$\beta$	0.66	-
Li diffusion coefficient in CAM	$D_{\text{CAM}}$	$7.3 \cdot 10^{-15}$	$\text{m}^2 \cdot \text{s}^{-1}$
stack pressure 392 MPa			
exchange current density	$j_0$	12.3	$\text{A} \cdot \text{m}^{-2}$
dependence of equilibrium potential on Li concentration in CAM	$dU/dc_{\text{Li}}$	$-3.6 \cdot 10^{-5}$	$\text{V} \cdot \text{m}^3 \cdot \text{mol}^{-1}$
prefactor of double layer CPE	$Q_{\text{DL}}$	1.05	$\text{F} \cdot \text{m}^{-2} \cdot \text{s}^{\beta-1}$
exponent of double layer CPE	$\beta$	0.72	-
Li diffusion coefficient in CAM	$D_{\text{CAM}}$	$6 \cdot 10^{-14}$	$\text{m}^2 \cdot \text{s}^{-1}$

$$C_{\text{DL}} = \frac{f_\omega}{R_{\text{CT}} \cdot \omega_{\text{max}}} \quad (7)$$

The factor  $f_\omega$  is unity for an ideal charge transfer semicircle at a planar electrode but deviates from unity in case of a TLM-type impedance of a composite electrode with  $R_{\text{ion}} \gg |Z_{\text{loc}}|$ , see supporting information. The obtained double layer capacitance  $C_{\text{DL}}$  increases from  $4.6 \cdot 10^{-7} \text{ F} \cdot \text{cm}^{-2}$  at 98 MPa to  $3.6 \cdot 10^{-6} \text{ F} \cdot \text{cm}^{-2}$  at 392 MPa. Note that these values are normalized by the surface area of the active material particles in the cathode.

In Figure 4a and b, we show the impedance spectra of the symmetrical cell In–Li | separator | In–Li and the single anode impedance after the correction of the separator resistance and the cable inductance, respectively. The exact procedure for the correction is given in the supporting information, see Figure S7. The In:Li atomic ratio in both electrodes was chosen as 60:40 in order to promote a stable In–Li | separator interface.<sup>[46]</sup> In Figure 4b, two semicircles are observable as also found in symmetrical cells with other SE as separator.<sup>[31,34]</sup> For the determination of the resistances of the two observable semicircles, a fit to the equivalent circuit shown in the inset of Figure 4b) was carried out in a frequency range of  $1.8 \cdot 10^4$  Hz to

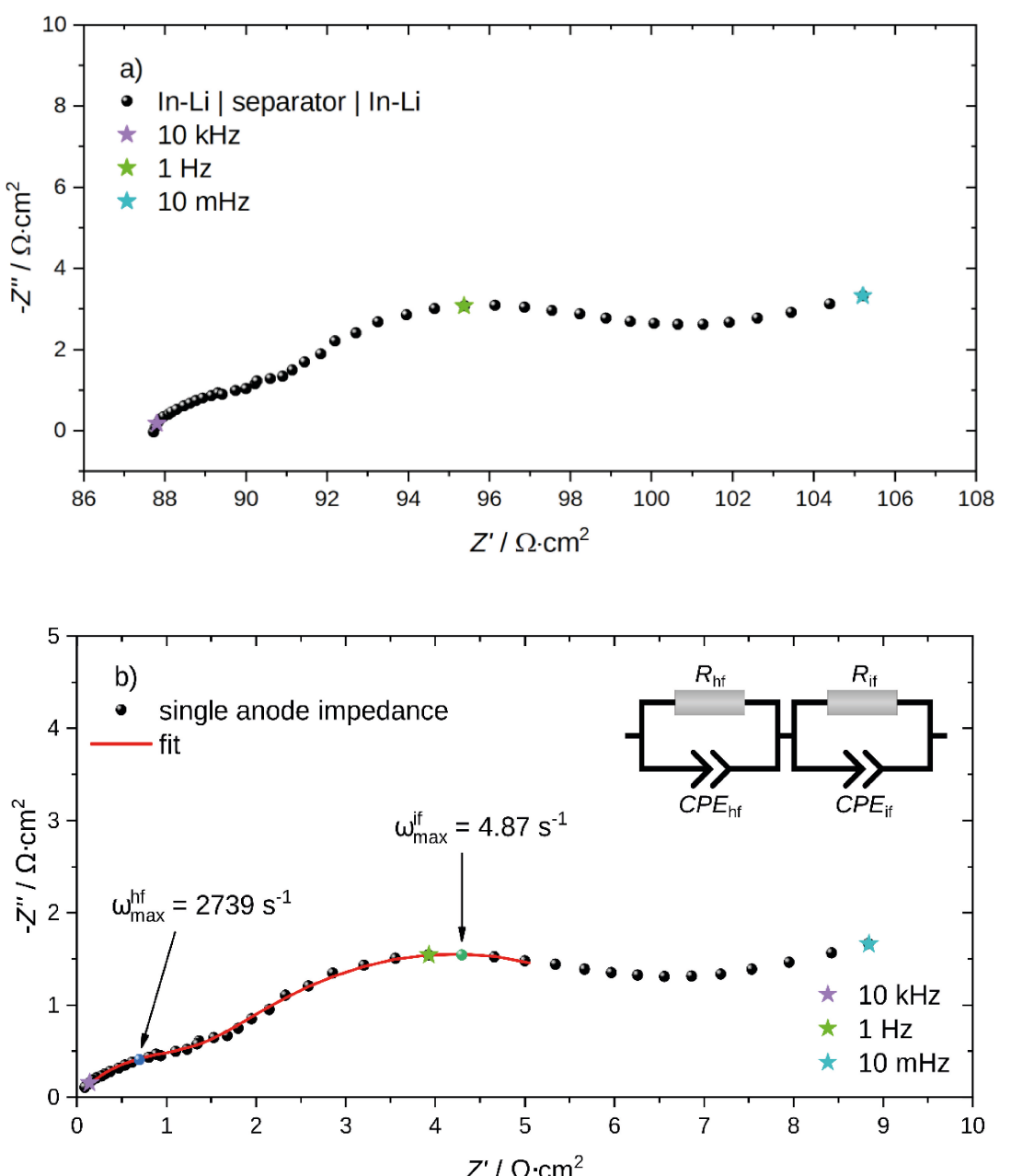


**Figure 4.** Impedance spectra (black circles) of a) symmetrical cell In–Li | separator | In–Li and b) single anode impedance obtained after subtracting the high-frequency resistance caused by the  $\text{LPSCIBr}_{0.7}$  separator layer and the inductance of the connecting cables. The red line in b) denotes a fit of the high-frequency and intermediate frequency regime of the spectrum to the equivalent circuit shown in the inset of Figure 4b.

$3.7 \cdot 10^{-1}$  Hz. In this case, all resistances are normalized to the area of the interface, which is identical to the nominal area of the cell. The capacitance related to the high-frequency semicircle was estimated from the angular frequency of the  $Z''$  maximum of the semicircle,  $\omega_{\max}^{\text{hf}}$ , and from the resistance  $R_{\text{hf}} = 1.4 \Omega \cdot \text{cm}^2$  using the equation:

$$C_{\text{hf}} = \frac{1}{R_{\text{hf}} \cdot \omega_{\max}^{\text{hf}}} \quad (8)$$

The capacitance of the intermediate-frequency semicircle ( $R_{\text{if}} = 5.8 \Omega \cdot \text{cm}^2$ ) was estimated in the same way

$$C_{\text{if}} = \frac{1}{R_{\text{if}} \cdot \omega_{\max}^{\text{if}}} \quad (9)$$

The obtained capacitance values are  $C_{\text{hf}} = 2.6 \cdot 10^{-4} \text{ F} \cdot \text{cm}^{-2}$  and  $C_{\text{if}} = 3.5 \cdot 10^{-2} \text{ F} \cdot \text{cm}^{-2}$ , respectively. A discussion of the underlying physical process will be given later.

The impedance spectrum of a full ASSB in a state of charge 50% and at a stack pressure of 392 MPa is shown in Figure 5. Here, three semicircles and a Warburg-type impedance at low frequencies are observable. The high-frequency resistance caused by the  $\text{LPSClBr}_{0.7}$  separator layer and the inductance of the connecting cables were subtracted as described in the supporting information, see Figure S8.

In Figure 6, we compare a Bode plot of the imaginary part of the impedance,  $Z''$ , for the full ASSB with the corresponding

Bode plot of the single anode impedance and the single cathode impedance. Since the composite cathode layers in the symmetric cells were slightly thinner than in the full ASSB cell (77  $\mu\text{m}$  vs. 88  $\mu\text{m}$ ), we simulated an impedance spectrum of an 88  $\mu\text{m}$  cathode by using the TLM (Eq. (1)) with the parameter values given in Tabs. 1 and 2, see Figure S9. This simulated spectrum is shown in Figure 6. The Bode plot of the full ASSB cell shows three  $Z''$  maxima corresponding to the three semicircles in Figure 5. The  $Z''$  maximum at the highest frequency (about 10<sup>4</sup> Hz) corresponds to the  $Z''$  maximum frequency of the cathode. This implies a remarkably fast charge transfer inside the cathode. We note that even in the case of lithium-ion batteries containing liquid electrolyte, lower maximum frequencies of the cathodic semicircle has been observed.<sup>[47]</sup> The  $Z''$  maximum around 10<sup>0</sup> Hz corresponds clearly to a  $Z''$  maximum of the anode. The  $Z''$  maximum at intermediate frequencies around 10<sup>2</sup> Hz seems to correspond to a  $Z''$  maximum of the anode. The slight frequency shift between the intermediate frequency  $Z''$  maximum of the full ASSB and that of the anode is most likely caused by the correction of the anode impedance spectrum at high frequencies.

The higher frequencies of the  $Z''$  maximum of the cathode as compared to the two maxima of the anode give indication that the processes at the interfaces between active materials and solid electrolyte particles are remarkably fast. In the following, we discuss these processes for both electrodes separately.

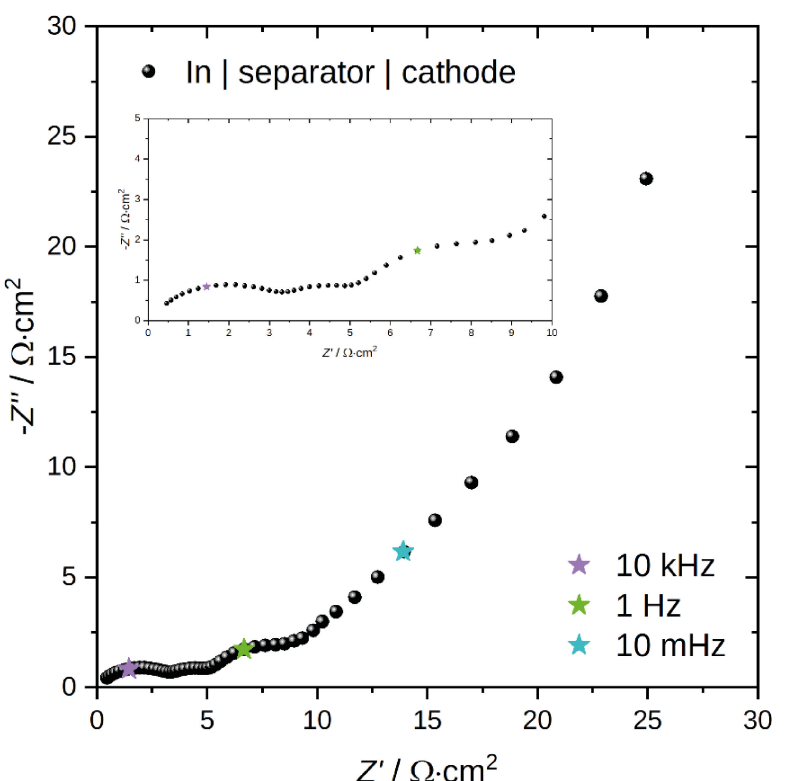


**Figure 5.** Impedance spectrum of a full ASSB taken at 50% state of charge (SOC50) during the second cycle at a stack pressure of 392 MPa. The high-frequency resistance caused by the  $\text{LPSClBr}_{0.7}$  separator layer and the inductance of connecting cables were subtracted. The frequency range extended from  $10^5$  to  $10^{-3}$  Hz. The inset shows a zoom into the high-frequency and intermediate-frequency range.

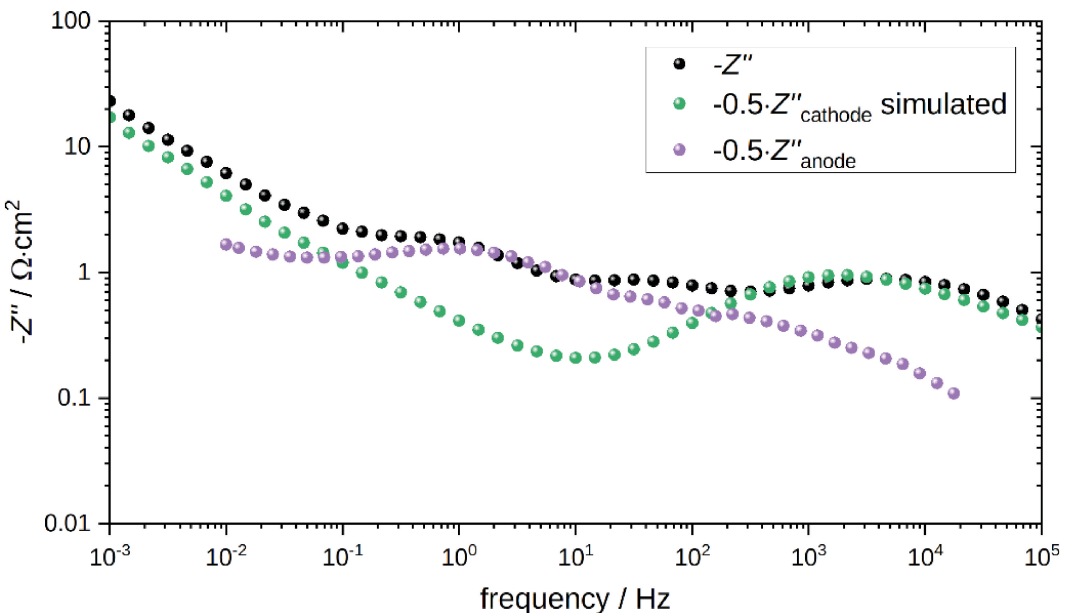
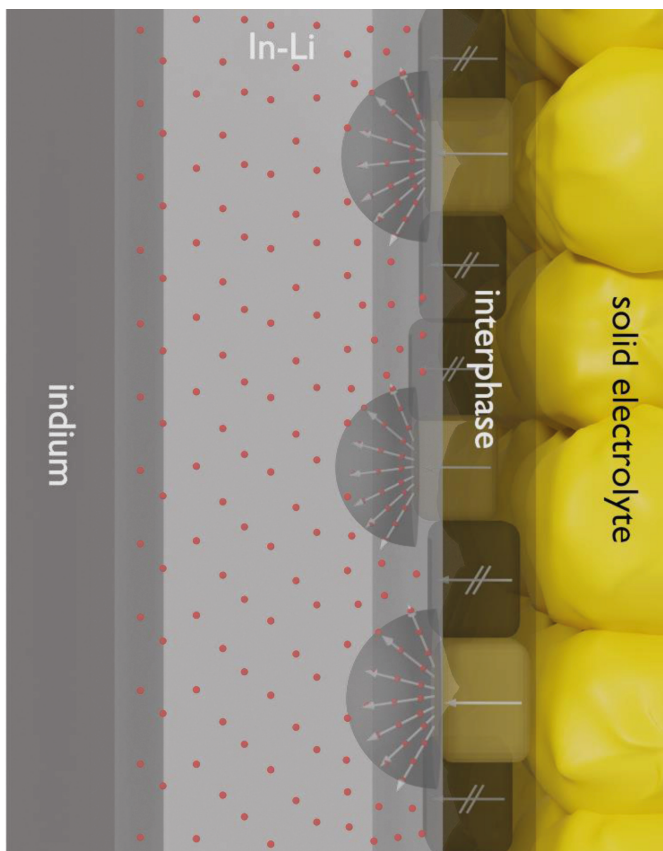


Figure 6. Bode plot of the imaginary impedance of the full ASSB (black) in comparison to a single anode (purple) and a single cathode (green).

The solid electrolyte is not stable in contact to the In–Li anode, leading to the formation of an interphase.<sup>[38]</sup> The high-frequency semicircle of the anode with a capacitance value of  $2.6 \cdot 10^{-4} \text{ F} \cdot \text{cm}^{-2}$  is most likely caused by the ion transport resistance of this interphase. The intermediate-frequency semicircle exhibits a much higher capacitance value of  $3.5 \cdot 10^{-2} \text{ F} \cdot \text{cm}^{-2}$  and should thus be related to chemical Li transport in the anode. In Ref. [26], an impedance semicircle at the solid electrolyte | metallic lithium interface was attributed to accumulation of Li vacancies in the metal close to the interface and the formation of Li voids. In case of the In–Li anode used here, the formation of such voids is unlikely. Therefore, the question arises why Li transport in the alloy anode leads to a semicircle and not to a Warburg-open-type impedance as in the case of the cathode. A semicircle points to a finite-length transport process. Indeed, such finite-length transport process take place in biphase materials, like In–Li alloys. In the case of an average composition In<sub>0.6</sub>Li<sub>0.4</sub> used here, two phases exist, namely In and In–Li.<sup>[46]</sup> The theory for Li intercalation into such a biphase material layer predicts an impedance semicircle due to Li transport with a time constant of  $\tau \approx \frac{(d_{\text{layer}} - d_{\text{In}})^2}{D_{\text{Li}}}.$ <sup>[48]</sup> Here,  $d_{\text{layer}}$  and  $d_{\text{In}}$  denote the thickness of the entire layer and of the un lithiated part of the layer, respectively, while  $D_{\text{Li}}$  is the Li diffusion coefficient in the lithiated part (in this case with composition In–Li). Consequently, the length scale  $\sqrt{D_{\text{Li}} \cdot \tau}$  should be identical to the thickness of the lithiated part of the layer,  $d_{\text{layer}} - d_{\text{In}}$ . Taking into account the average composition In<sub>0.6</sub>Li<sub>0.4</sub>, the molar masses and densities of Li,<sup>[49]</sup> In<sup>[49]</sup> and In–Li<sup>[50]</sup> as well as the used amount of In foil (25 mg), the thickness of the lithiated part of the layer,  $d_{\text{layer}} - d_{\text{In}}$ , is in the range of 50  $\mu\text{m}$ . The Li diffusion coefficient in In–Li is in the range of  $10^{-9} \text{ cm}^2/\text{s}.$ <sup>[51]</sup> From the frequency of the  $Z''$  maximum,  $\nu^*$ , being in the range of a few Hz, a time scale of  $\tau = 1/(2\pi\nu^*) \approx 0.1 \text{ s}$

can be deduced. This results in a length scale  $\sqrt{D_{\text{Li}} \cdot \tau} \approx 100 \text{ nm}$ , indicating a transport length significantly lower than 50  $\mu\text{m}$ . Consequently, we propose the following transport mechanism, which is illustrated in Figure 7. The interphase formed due to decomposition of the solid electrolyte is laterally heterogeneous, and Li<sup>+</sup> ion transport across the interphase takes place mainly in regions with low ion transport resistance. Thus, the Li<sup>+</sup> ions enter the In–Li phase in these regions, leading to a localized transport resistance around these regions.

In the case of the cathode, the capacitance values related to the semicircle were estimated as  $0.46 \text{ F} \cdot \text{cm}^{-2}$  at 98 MPa to  $3.6 \text{ F} \cdot \text{cm}^{-2}$  at 392 MPa, respectively, and thus lower than the capacitance related to the high-frequency semicircle of the anode. For amorphous LiNbO<sub>3</sub>, relative permittivities in the range of  $\epsilon_{\text{LiNbO}_3} \approx 50$  have been reported.<sup>[52]</sup> The thickness of LiNbO<sub>3</sub> coatings of CAM particles are typically in a range from  $d=5\text{--}10 \text{ nm}.$ <sup>[53\text{--}55]</sup> The area-specific capacitance of the coating,  $C_{\text{LiNbO}_3} = \epsilon_0 \cdot \epsilon_{\text{LiNbO}_3} / d$ , should thus be in the range of  $4.5\text{--}9 \text{ F} \cdot \text{cm}^{-2}$ , which is close to the capacitance value estimated for 392 MPa. This indicates that at 392 MPa, the complete surface of the LiNbO<sub>3</sub> coating is in good contact to solid electrolyte particles, and the capacitance of the interface is governed by the LiNbO<sub>3</sub> capacitance. At 98 MPa, the capacitance estimated from the impedance spectra is about one order of magnitude lower, suggesting that the LiNbO<sub>3</sub> coating is only in partial contact to the solid electrolyte particles. Nevertheless, the exchange current density at 98 MPa,  $j_0 = 2.0 \text{ A} \cdot \text{m}^{-2}$ , is high and comparable to values obtained at CAM | liquid electrolyte interfaces. Despite the incomplete contact between CAM particles and SE particles, a Warburg-short-type impedance is not observed at low frequencies, but a Warburg-open-type impedance. This suggests the following transport scenario illustrated in Figure 8. At 98 MPa, the solid electrolyte particles



**Figure 7.** Schematic 3D illustration of transport processes taking place at the anode | separator interface. The interphase formed due to decomposition of the solid electrolyte is laterally heterogeneous, and  $\text{Li}^+$  ion transport across the interphase takes place mainly in regions with low ion transport resistance (light brown regions). Other regions of the interphase (dark brown regions) are ion blocking. Thus, the  $\text{Li}^+$  ions enter the In-Li phase at the interface to interphase regions with low ion transport resistance, leading to a finite-length transport resistance in the In-Li phase.

are in partial contact to the  $\text{LiNbO}_3$  coating on the CAM particles. Amorphous  $\text{LiNbO}_3$  is a  $\text{Li}^+$  ion conductor with a relatively high  $\text{Li}^+$  ion conductivity in the range of  $10^{-6}$  S/cm.<sup>[56]</sup> The characteristic time scale for ion transport in  $\text{LiNbO}_3$  is given by  $\tau = R_{\text{LiNbO}_3} \cdot C_{\text{LiNbO}_3} = \varepsilon_0 \cdot \varepsilon_{\text{LiNbO}_3} / \sigma_{\text{LiNbO}_3} \approx 4 \cdot 10^{-6}$  s. This time scale is only slightly shorter than the time constant of the cathode semicircle ( $\approx 10^{-5}$  s), suggesting that fast ion transport in the  $\text{LiNbO}_3$  layer is an important prerequisite for fast charge transfer of  $\text{Li}^+$  ions from the SE particles into the CAM particles. As seen from the low-frequency Warburg-open-type impedance for the cathode in Figure 6, Li chemical diffusion in the CAM particles is much slower than  $\text{Li}^+$  charge transfer. Due to the fast transport inside the  $\text{LiNbO}_3$  layer, this layer should be capable of conducting  $\text{Li}^+$  ions to the entire interface between  $\text{LiNbO}_3$  and CAM particles, and the subsequent  $\text{Li}^+$  transfer from the  $\text{LiNbO}_3$  layer into the CAM particles should thus take place homogeneously over this interface. Consequently, there should be homogeneous Li diffusion in the CAM particles and no local finite-length diffusion processes as inside the In-Li anode. This results in a Warburg-open-type impedance for the

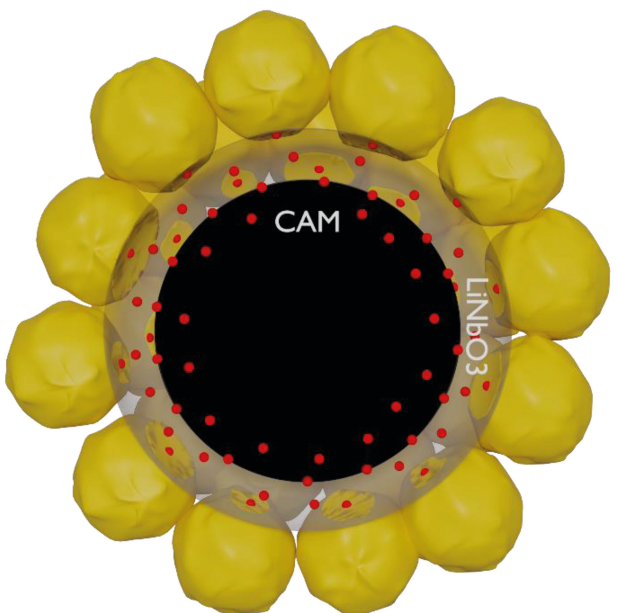


**Figure 8.** Schematic 3D illustration of transport processes taking place at the interface between cathode active material particles (CAM) coated with a  $\text{LiNbO}_3$  layer and solid electrolyte particles. Although there is only partial contact between solid electrolyte particles and  $\text{LiNbO}_3$  layer, the  $\text{Li}^+$  ions are conducted to the entire interface between  $\text{LiNbO}_3$  and CAM particles.

cathode in contrast to the Warburg-short-type impedance of the anode.

Thus, our results indicate that the distinct impedance contributions of anode and cathode are closely related to the distinct properties of interphases in these electrodes, i.e., a laterally heterogeneous interphase formed during decomposition of the solid electrolyte at the In-Li anode vs. a homogeneously coated  $\text{LiNbO}_3$  layer coated onto the cathode active material particles. While this explains the qualitative differences between anode and cathode impedance, the quantitative understanding of the remarkably low charge transfer resistance between CAM particles and SE particles in the composite cathode require more detailed studies of the atomic structure at CAM/SE interfaces in the future, e.g. by high-resolution electron microscopy.

## Conclusions

We have compared the impedance spectra of a full ASSB with the spectra of symmetric cells composite cathode | separator | composite cathode and In-Li anode | separator | In-Li anode. The obtained results show that the high-frequency semicircle and the low-frequency Warburg impedance of the full ASSB originate from the cathode impedance, while the intermediate-frequency and low-frequency semicircle originate from the anode impedance. We propose transport mechanisms for both electrodes, in which the distinct properties of interphases at these electrodes play an important role. At the anode | separator interface, a laterally inhomogeneous interphase formed during decomposition of the solid electrolyte at the

In–Li anode causes a localized chemical diffusion of Li inside the In–Li alloy. The time constant of the Warburg-short-type impedance in the range of  $10^{-2}$  s is determined by the length scale of lateral heterogeneities in the interphase and the chemical Li diffusion coefficient in the In–Li phase of the alloy. Inside the cathode, the  $\text{LiNbO}_3$  layer coated onto the CAM particles acts as an artificial interphase with relative high  $\text{Li}^+$  ion conductivity. Due to the fast transport in the  $\text{LiNbO}_3$  layer,  $\text{Li}^+$  ions reach the entire surface of the CAM particles, even if the surrounding SE particles are only in partial contact to the  $\text{LiNbO}_3$  layer. This results in a homogeneous Li diffusion in the CAM particles. Fast transport in the  $\text{LiNbO}_3$  layer is thus an important prerequisite for the short time scale of the cathode impedance semicircle in the range of  $10^{-5}$  s.

## Associated Content

**Supporting Information:** XRD pattern and ionic conductivity of the glass-ceramic (gc) solid electrolyte prepared by high-energy dry ball milling (HDM); SEM image and particle size distribution of the polycrystalline  $\text{LiNi}_{0.85}\text{Co}_{0.10}\text{Mn}_{0.05}\text{O}_2$  (NCM851005); Starting value of the thermodynamic parameter  $dU/dc_{\text{Li}}$  for the transmission-line model fit; Subtraction of separator resistance and cable inductance from the impedance spectra of the symmetric cells: composite cathode | separator | composite cathode; Subtraction of separator resistance and cable inductance from the impedance spectra of the symmetric cell: In–Li | separator | In–Li; Subtraction of separator resistance and cable inductance from the impedance spectra of the ASSB at SOC50 and a stack pressure of 392 MPa; Thickness correction of the single cathode impedance at a stack pressure of 392 MPa; Calculation of the frequency factor  $f_\omega$  for an ideal composite electrode in the framework of the transmission-line model; Schematic illustration of the fabrication procedure for both types of symmetric cells.

## Acknowledgements

Financial support of this work by the German Science Foundation (DFG) is gratefully acknowledged. We thank Dr. Vanessa Miß for capturing the SEM image of the active material particles. Open Access funding enabled and organized by Projekt DEAL.

## Conflict of Interests

The authors declare no conflict of interest.

## Data Availability Statement

The data that support the findings of this study are available from the corresponding author upon reasonable request.

**Keywords:** Interphases · composite electrodes · all-solid-state battery · symmetrical cells

- [1] O. Ruhnau, S. Bannik, S. Otten, A. Praktiknjo, M. Robinius, *Energy* **2019**, *166*, 989–999.
- [2] I. Jonek-Kowalska, *Resour. Policy* **2022**, *77*, 102701.
- [3] F. H. Gandoman, J. Jaguemont, S. Goutam, R. Gopalakrishnan, Y. Firouz, T. Kalogiannis, N. Omar, J. van Mierlo, *Appl. Energy* **2019**, *251*, 113343.
- [4] M. S. Whittingham, *Nano Lett.* **2020**, *20*, 8435–8437.
- [5] T. Xu, W. Wang, M. L. Gordin, D. Wang, D. Choi, *JOM* **2010**, *62*, 24–30.
- [6] H. S. Hirsh, Y. Li, D. H. S. Tan, M. Zhang, E. Zhao, Y. S. Meng, *Adv. Energy Mater.* **2020**, *10*, 2001274.
- [7] J. B. Quinn, T. Waldmann, K. Richter, M. Kasper, M. Wohlfahrt-Mehrens, *J. Electrochim. Soc.* **2018**, *165*, A3284–A3291.
- [8] P. Sun, R. Bisschop, H. Niu, X. Huang, *Fire Technol.* **2020**, *56*, 1361–1410.
- [9] A. Lecocq, G. G. Eshetu, S. Grugeon, N. Martin, S. Laruelle, G. Marlair, *J. Power Sources* **2016**, *316*, 197–206.
- [10] M. Shoji, E. J. Cheng, T. Kimura, K. Kanamura, *J. Phys. D* **2019**, *52*, 103001.
- [11] Z. Ma, H.-G. Xue, S.-P. Guo, *J. Mater. Sci.* **2018**, *53*, 3927–3938.
- [12] J. Zhou, T. Qian, J. Liu, M. Wang, L. Zhang, C. Yan, *Nano Lett.* **2019**, *19*, 3066–3073.
- [13] P. Vadhra, J. Hu, M. J. Johnson, R. Stocker, M. Braglia, D. J. L. Brett, A. J. E. Rettie, *ChemElectroChem* **2021**, *8*, 1930–1947.
- [14] J. Schnell, T. Günther, T. Knoche, C. Vieider, L. Köhler, A. Just, M. Keller, S. Passerini, G. Reinhart, *J. Power Sources* **2018**, *382*, 160–175.
- [15] C. Wang, J. Liang, Y. Zhao, M. Zheng, X. Li, X. Sun, *Energy Environ. Sci.* **2021**, *14*, 2577–2619.
- [16] K. J. Kim, M. Balaish, M. Wadaguchi, L. Kong, J. L. M. Rupp, *Adv. Energy Mater.* **2021**, *11*, 2002689.
- [17] X. Yu, R. Chen, L. Gan, H. Li, L. Chen, *Engineering* **2023**, *21*, 9–14.
- [18] S. V. Patel, S. Banerjee, H. Liu, P. Wang, P.-H. Chien, X. Feng, J. Liu, S. P. Ong, Y.-Y. Hu, *Chem. Mater.* **2021**, *33*, 1435–1443.
- [19] Y. Kato, S. Hori, T. Saito, K. Suzuki, M. Hirayama, A. Mitsui, M. Yonemura, H. Iba, R. Kanno, *Nat. Energy* **2016**, *1*, 16030.
- [20] N. Kamaya, K. Homma, Y. Yamakawa, M. Hirayama, R. Kanno, M. Yonemura, T. Kamiyama, Y. Kato, S. Hama, K. Kawamoto, A. Mitsui, *Nat. Mater.* **2011**, *10*, 682–686.
- [21] Y.-G. Lee, S. Fujiki, C. Jung, N. Suzuki, N. Yashiro, R. Omoda, D.-S. Ko, T. Shiratsuchi, T. Sugimoto, S. Ryu, J. H. Ku, T. Watanabe, Y. Park, Y. Aihara, D. Im, I. T. Han, *Nat. Energy* **2020**, *5*, 299–308.
- [22] D. H. S. Tan, Y.-T. Chen, H. Yang, W. Bao, B. Sreenarayanan, J.-M. Doux, W. Li, B. Lu, S.-Y. Ham, B. Sayahpour, J. Scharf, E. A. Wu, G. Deysher, H. E. Han, J. H. Jahn, H. Jeong, J. B. Lee, Z. Chen, Y. S. Meng, *Science* **2021**, *373*, 1494–1499.
- [23] W. Zhang, F. H. Richter, S. P. Culver, T. Leichtweiss, J. G. Lozano, C. Dietrich, P. G. Bruce, W. G. Zeier, J. Janek, *ACS Appl. Mater. Interfaces* **2018**, *10*, 22226–22236.
- [24] X. Sun, Y. Yamada, S. Hori, Y. Li, K. Suzuki, M. Hirayama, R. Kanno, *J. Mater. Chem. A* **2021**, *9*, 17905–17912.
- [25] C. Sedlmeier, R. Schuster, C. Schramm, H. A. Gasteiger, *J. Electrochim. Soc.* **2023**, *170*, 30536.
- [26] R. Schlenker, D. Stępień, P. Koch, T. Hupfer, S. Indris, B. Roling, V. Miß, A. Fuchs, M. Wilhelmi, H. Ehrenberg, *ACS Appl. Mater. Interfaces* **2020**, *12*, 20012–20025.
- [27] G. Fukunishi, A. Ikezawa, T. Okajima, F. Kitamura, K. Suzuki, M. Hirayama, R. Kanno, H. Arai, *ACS Appl. Energ. Mater.* **2023**, *6*, 10908–10917.
- [28] G. Fukunishi, M. Tabuchi, A. Ikezawa, T. Okajima, F. Kitamura, K. Suzuki, M. Hirayama, R. Kanno, H. Arai, *J. Power Sources* **2023**, *564*, 232864.
- [29] W. Zhang, D. A. Weber, H. Weigand, T. Arlt, I. Manke, D. Schröder, R. Koerver, T. Leichtweiss, P. Hartmann, W. G. Zeier, J. Janek, *ACS Appl. Mater. Interfaces* **2017**, *9*, 17835–17845.
- [30] A. Sakuda, A. Hayashi, M. Tatsumisago, *Chem. Mater.* **2010**, *22*, 949–956.
- [31] S. Hori, R. Kanno, X. Sun, S. Song, M. Hirayama, B. Hauck, M. Dippon, S. Dierickx, E. Ivers-Tiffée, *J. Power Sources* **2023**, *556*, 232450.
- [32] A. Ikezawa, G. Fukunishi, T. Okajima, F. Kitamura, K. Suzuki, M. Hirayama, R. Kanno, H. Arai, *Electrochim. Commun.* **2020**, *116*, 106743.
- [33] M. Cronau, M. Szabo, B. Roling, *Mater Adv* **2021**, *2*, 7842–7845.
- [34] V. Miß, A. Ramanayagam, B. Roling, *ACS Appl. Mater. Interfaces* **2022**, *14*, 38246–38254.
- [35] P. Minnmann, L. Quillman, S. Burkhardt, F. H. Richter, J. Janek, *J. Electrochim. Soc.* **2021**, *168*, 40537.
- [36] C. König, V. Miß, L. Janin, B. Roling, *ACS Appl. Energ. Mater.* **2023**, *6*, 9356–9362.

- [37] U. Schwarz, S. Bräuninger, K. Syassen, R. Kniep, *J. Solid State Chem.* **1998**, *137*, 104–111.
- [38] S. Luo, Z. Wang, X. Li, X. Liu, H. Wang, W. Ma, L. Zhang, L. Zhu, X. Zhang, *Nat. Commun.* **2021**, *12*, 6968.
- [39] A.-Y. Kim, F. Strauss, T. Bartsch, J. H. Teo, T. Hatsukade, A. Mazilkin, J. Janek, P. Hartmann, T. Brezesinski, *Chem. Mater.* **2019**, *31*, 9664–9672.
- [40] M. Cronau, M. Duchardt, M. Szabo, B. Roling, *Batteries & Supercaps* **2022**, *5*.
- [41] S. Wang, M. Yan, Y. Li, C. Vinado, J. Yang, *J. Power Sources* **2018**, *393*, 75–82.
- [42] M. Ménétrier, I. Saadoune, S. Levasseur, C. Delmas, *J. Mater. Chem.* **1999**, *9*, 1135–1140.
- [43] S. Cui, Y. Wei, T. Liu, W. Deng, Z. Hu, Y. Su, H. Li, M. Li, H. Guo, Y. Duan, W. Wang, M. Rao, J. Zheng, X. Wang, F. Pan, *Adv. Energy Mater.* **2016**, *6*, 1501309.
- [44] Y. Wei, J. Zheng, S. Cui, X. Song, Y. Su, W. Deng, Z. Wu, X. Wang, W. Wang, M. Rao, Y. Lin, C. Wang, K. Amine, F. Pan, *J. Am. Chem. Soc.* **2015**, *137*, 8364–8367.
- [45] O. Chaouachi, J.-M. Réty, S. Génies, M. Chandesris, Y. Bultel, *Electrochim. Acta* **2021**, *366*, 137428.
- [46] A. L. Santhosha, L. Medenbach, J. R. Buchheim, P. Adelhelm, *Batteries & Supercaps* **2019**, *2*, 524–529.
- [47] M. Cronau, A. Paulus, L. P. Pescara, M. Kroll, D. Renz, J. A. Mekontso, A. Marx, B. Roling, *Batteries & Supercaps* **2022**, *5*, e202200194.
- [48] P. Gamblire, K. S. Hariharan, A. Khandelwal, V. S. Kumar, S. M. Kolake, D. Oh, S. Doo, *J. Electrochem. Soc. Interface* **2014**, *161*, A183–A193.
- [49] W. M. Haynes, Ed. *CRC handbook of chemistry and physics: A ready-reference book of chemical and physical data*, 93. ed.; CRC Press/Taylor & Francis Group, 2012.
- [50] H. Ehrenberg, H. Pauly, T. Hansen, J.-C. Jaud, H. Fuess, *J. Solid State Chem.* **2002**, *167*, 1–6.
- [51] Y. Lu, C.-Z. Zhao, R. Zhang, H. Yuan, L.-P. Hou, Z.-H. Fu, X. Chen, J.-Q. Huang, Q. Zhang, *Sci. Adv.* **2021**, *7*, eabi5520.
- [52] S. H. Kim, M. S. Jang, B. G. Chae, Y. S. Yang, *J. Korean Phys. Soc.* **1998**, *32*, S807–S810.
- [53] L. Peng, H. Ren, J. Zhang, S. Chen, C. Yu, X. Miao, Z. Zhang, Z. He, M. Yu, L. Zhang, S. Cheng, J. Xie, *Energy Storage Mater.* **2021**, *43*, 53–61.
- [54] X. Sun, S. Hori, Y. Li, Y. Yamada, K. Suzuki, M. Hirayama, R. Kanno, *J. Mater. Chem. A* **2021**, *9*, 4117–4125.
- [55] N. Ohta, K. Takada, I. Sakaguchi, L. Zhang, R. Ma, K. Fukuda, M. Osada, T. Sasaki, *Electrochem. Commun.* **2007**, *9*, 1486–1490.
- [56] P. Heitjans, M. Masoud, A. Feldhoff, M. Wilkening, *Faraday Discuss.* **2007**, *134*, 67–82.

Manuscript received: December 6, 2023

Revised manuscript received: February 15, 2024

Accepted manuscript online: February 16, 2024

Version of record online: March 1, 2024